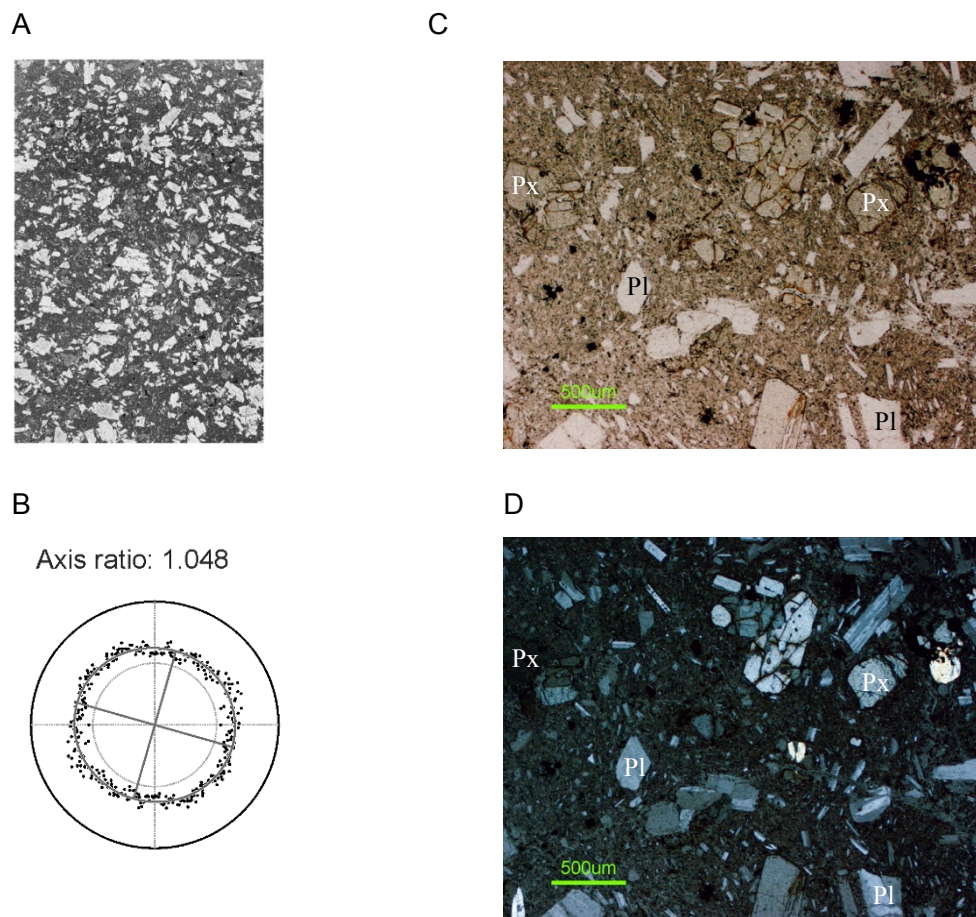


## Supporting online material

### *Reconstructing magma failure and the degassing network of dome-building eruptions*

#### 1. VOLCANIC MATERIAL

The material chosen was a volcanic rock from dome-building eruptions at Volcán de Colima in Mexico, as extensive experimental work has been performed on this rock type (e.g., Lavallée et al., 2007; 2008; 2012b). The dome rock is an andesite with approximately 55 +/- 5 vol.% of commonly euhedral crystals of plagioclase and pyroxene up to 2.5 mm in length. Embedded microlites showed minor signs of flow alignment, but the crystalline assemblage was characterized as nearly isotropic with an axis ratio of 1.048 (Fig. DR1; Lavallée et al., 2008). The rock has an average connected porosity of 6.9 vol.% and is highly degassed ( $\leq 0.1 \pm 0.05\%$ ); no volatiles were lost during the extensive heat treatment as confirmed by weight loss tests before and after treatment (Lavallée et al., 2007). Geothermometry has described the pre-eruptive magma condition to 960-1020 °C (Reubi and Blundy, 2008; Savov et al., 2008), whereas the glass transition has been estimated at approximately 710 °C (Lavallée et al., 2012a), although no deformation was experimentally noted below 850 °C (Lavallée et al., 2007).



**Figure DR1. Petrography and microstructures of dome lava samples.** (A) Photograph of a thin section (the crystals appear in white and pale grey colours, and interstitial glass as black) from which (B) the anisotropy was measured (Lavallée et al., 2008). The graph is a direction vs slope plot for the intersection of segments with the analysed fabric. Each ring is equivalent to a count of 500 units (see Gerik and Kruhl, 2008). The starting material displays a low anisotropy of 4.8%. Alongside, microphotograph under C) transmitted light and D) cross nickel polarised light show examples of the microstructures present in an original, undeformed sample. Px: pyroxene; Pl: plagioclase

## 2. DEFORMATION EXPERIMENTS

We have conducted a series of experiments in which dome lavas samples from Volcán de Colima (Mexico) were deformed using a stiff, servo-controlled uniaxial press operating under constant load ( $<300$  kN) and high temperature ( $<1300$  °C), and equipped with a fast-acquisition acoustic monitoring system (Hess et al., 2007; Lavallée et al., 2008) (Fig. DR2). For the experiments reported here, samples of 50x25 mm and 80x40 mm (length x diameter) were prepared using a diamond coring drill, with the end faces ground flat and parallel to within 0.01 mm. The connected porosity as well as P- and S-wave velocity of the prepared samples was analysed before and after each experiment (see section 4 and 5 below). The samples were placed between the pistons and heated to  $940 \pm 2$  °C using a 12 kW, three-zone split cylinder furnace. After thermal equilibration (over a period of 9 hours), the samples were deformed under constant loads up to different strain increments or until complete failure. Note: Although strain and stress distribution (owing to friction along the sample-piston interface) are not homogeneous throughout the sample (Fig. DR3), the systematic uniaxial conditions permit the comparison of experimental products with increasing applied stresses.

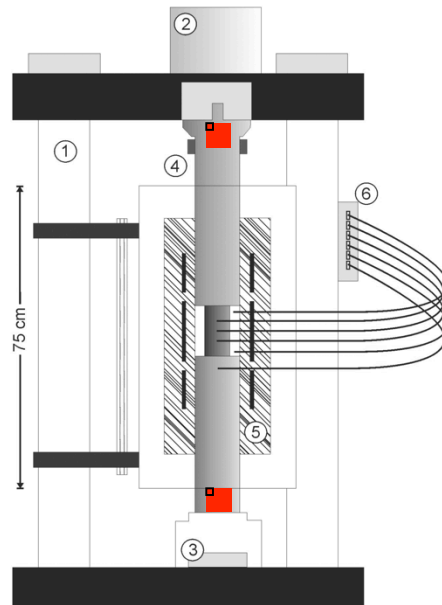


**Figure DR2. Sketch of the uniaxial press:** (1) load frame; (2) servo cylinder with LVDT; (3) load cell; (4) cooling jacket; (5) 3-zone split cylinder furnace; and (6) 6-input thermocouple interface (for type K and S). The red squares show the locations of the AE sensors at the cool ends of the pistons (Modified from Hess et al., 2007).

Here, we focus on moderate to high applied stresses ( $\geq 20$  MPa) as deformation below such load has been reported to be purely ductile with viscous and plastic components (Lavallée et al., 2007). Such low-stress deformation of magma has been reported to results in constant strain rate and is essentially aseismic, except for the sparse occurrence of AE associated with the sporadic fracture of larger crystals and agglomerations (Lavallée et al., 2008). The porosity and ultrasonic velocity of magma remained largely unchanged by such deformation (see Table DR2). Post-experiment microscopic analysis has revealed the reorientation of crystals and a near absence of

fracture or crystal dislocation, highlighting the crystal-plastic and viscous nature of magma deformation under these conditions (Lavallée et al., 2008).

Under the range of conditions investigated in this study ( $\geq 20$  MPa), deformation is accompanied by acceleration in resultant strain rate (Fig. DR4). With increased applied stresses the strain rate is higher and acceleration faster. Within the imposed strain limit of 35% (see Hess et al., 2007), the sample deformed at 20 MPa did not proceed to fail; although the edge of the sample evidence cracking due to bulging after 20% strain (Fig. DR3A). Experiments performed at higher applied stresses did succumb to failure.

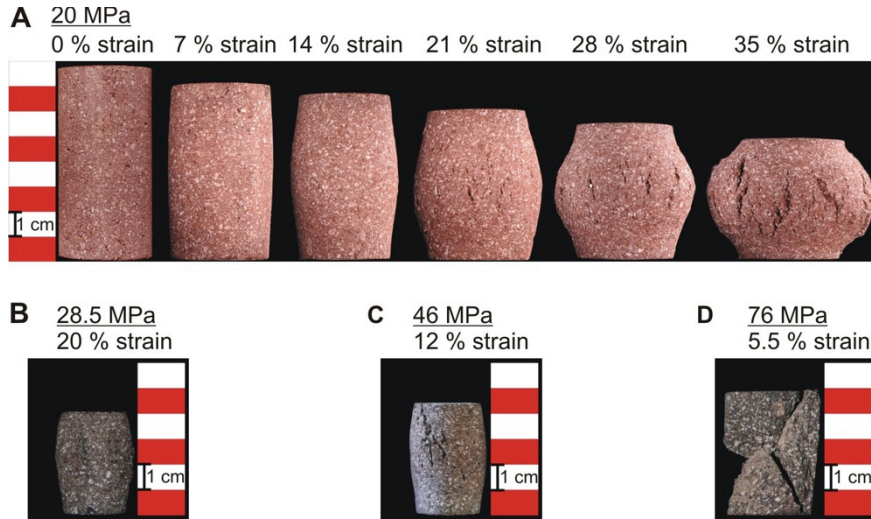


**Figure DR3. Magma deformation and failure.** (A) Strain-step evolution of macroscopic extensional crack propagation during deformation under an applied stress of 20 MPa. Photograph of samples deformed under applied stresses of (B) 28.5 MPa, (C) 46 MPa and (D) 76 MPa.

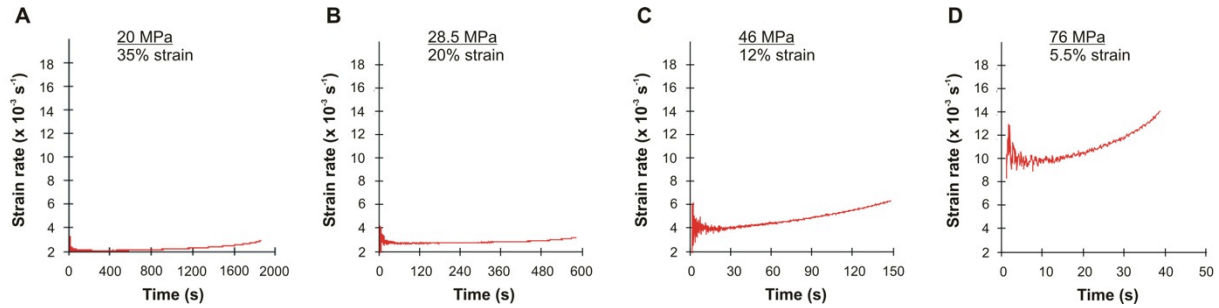


**Figure DR4. Mechanical response of magma to applied stress.** The graphs show the evolution of the strain rate for deformation at applied stresses of A) 20 MPa, B) 28.5 MPa, C) 46 MPa and D) 76 MPa.

### 3. ACOUSTIC EMISSION MONITORING AND ANALYSIS

Acoustic emissions (AEs) were measured using two piezoelectric transducers (Wideband type WD, Physical Acoustic Corporation) mounted at the end of the loading rams (acting as waveguides). AE signals were pre-amplified by 40 dB and recorded by a fast-acquisition PCI-2 AE recorder at 10 MHz sampling frequency using a triggering criterion of 50 dB simultaneously across both transducers, and with a common event arrival time difference of 150  $\mu$ s or less.

To further analyse our combined AE dataset, we conducted a seismic *b*-value analysis. In monitoring seismically active regions, one of the most useful analyses to gauge the degree and

evolution of fracturing is the seismic  $b$ -value, defined as the statistical gradient of the number of events of a certain magnitude; that is, the Log(AE frequency)-magnitude distribution (Aki, 1965, 1967). This measure provides a statistical bound on the number of events of a defined size, which – in the laboratory – can be used to ascertain the likelihood of violent and rapid failure or of more benign behaviour; information useful to volcano hazard mitigation (McNutt, 2005). The  $b$ -value serves to describe the extent of crack propagation, where a general decrease in calculated  $b$ -values reflects the formation of longer shear planes (Lavallée et al., 2008). Deformation of our samples across the ductile-brittle transition is accompanied by a decrease of the  $b$ -value from 3.6 at 28.5 MPa to 2.4 at 76 MPa (Fig. DR5), which suggests an increased fracture localisation with applied stress. In other word, deformation at higher applied stress generates larger fractures of higher amplitude.

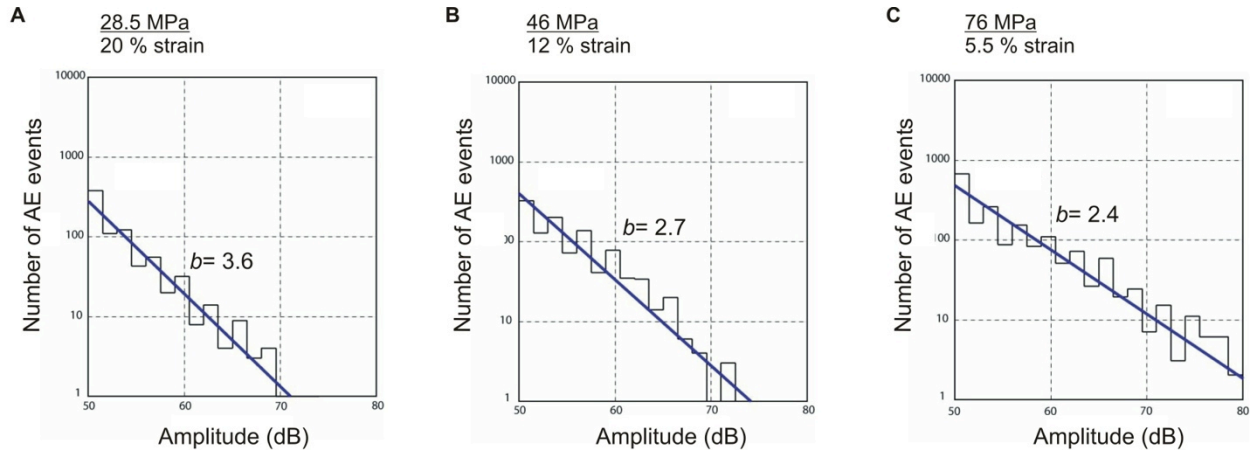


**Figure DR5. Frequency distribution of acoustic emission event amplitude.** The negative slope of the distribution, referred to as the  $b$ -value, provides a statistical gradient of the size of acoustic events and thus quantitatively assess the relative proportion of small to large fractures. We note that the  $b$ -value decreases with an increase applied stress

In volcanic hazard assessment, forecasting the timing of an eruption is fundamental to our ability at mitigating the risk. It has recently been suggested that the failure of magma can be forecasted via the failure forecast method (FFM) put forth by Voight (1988). Here we assess that this method may be applied to the extent of the ductile-brittle transition. The FFM relies on the production rate of precursory phenomena (e.g., seismicity rate, AE rate, seismic energy release, etc.) and correlating their accelerations to the likeliness of failure via the equation

$$\frac{d^2\Omega}{dt^2} = A \left( \frac{d\Omega}{dt} \right)^\alpha \quad (1)$$

where  $d^2\Omega/dt^2$  and  $d\Omega/dt$  are the acceleration and rate of the phenomenon being monitored (here AE), and  $A$  and  $\alpha$  are empirically determined parameters (Kilburn, 2003; Voight, 1988). More explicitly  $\alpha$  is expected to evolve from 1 to 2 before an eruption (Cornelius and Voight, 1995). Recent description of the fracturing time series that arise from random energy fluctuations within a finite volume subject to a constant remote stress proposed that the peaks in event rate (rather than all seismic events) predict best the path to failure and that  $\alpha = 2$  when approaching failure (Kilburn, 2003). The equation can thus be simplified to:

$$\frac{1}{d\Omega/dt} = A(t_f - t) \quad (2)$$



where  $t_f$  is the expected time-to-failure. Since the acceleration increases before failure, the extrapolation of the inverse rate to zero provides the time-to-failure (Fig. DR6). In our failure analysis, we compared the accuracy using 50% and 100% of the dataset and found equal accuracy of the method. We find that despite the fact that the time window for forecasting failure at higher applied stress diminishes (Fig. S6), the accuracy of the forecast remains whether we use 50% of the data or the whole dataset (Table S1).

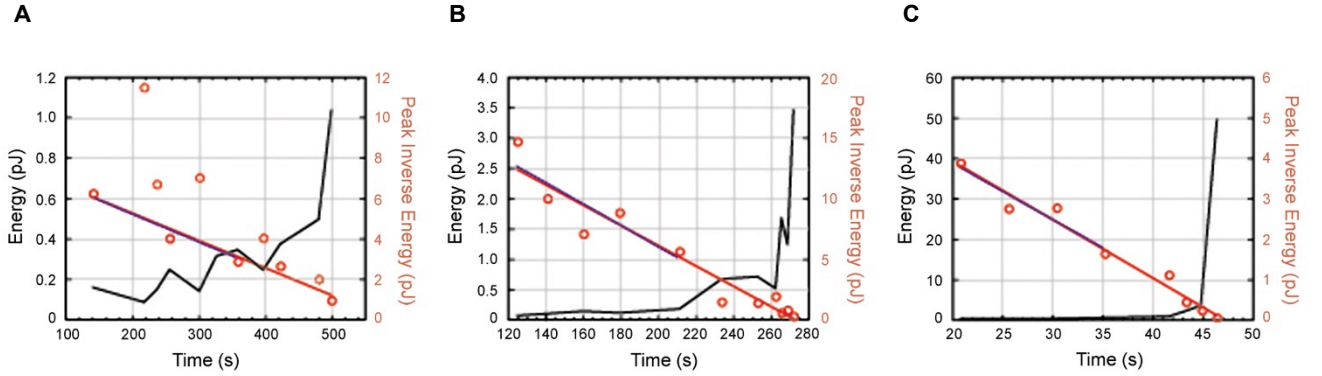


**Figure DR6. Forecasting magma failure across the ductile-brittle transition.** The graphs report the acceleration in released AE energy (black line) for deformation at (A) 28.5 MPa, (B) 46 MPa and (C) 76 MPa. Forecasts are based on the extrapolation (blue and red lines) of peaks in inverted rate of released AE energy (red circles). The inverted peak rates were calculated by binning the number of AE data by time interval for a higher accuracy of the method (Smith and Kilburn, 2010). Comparison of forecast time after 50 % of the deformation ( $F_{50}$ ; red line) to the forecast time using all inverse seismic rate (blue dotted line) are used to test the accuracy of the method in forecasting the failure of magma (compiled in Table S1). The estimated  $b$ -value decrease reflects the increasing localisation of crack propagation with increasing applied stress (see Fig. S5).

**Table DR1.** Accuracy of the failure forecasts using the AE output from the first 50% strain ( $F_{50}$ ) and the entire dataset ( $F_{100}$ ). Variation in accuracy is approximately 0.1 percentage points (based upon 0.1s accuracy)

Applied stress (MPa)	Failure (s)	$F_{50}$ (s)	Accuracy (%)	$F_{100}$ (s)	Accuracy (%)
28.5	587	578.6	1.4	589.3	0.4
46	273	268.8	1.5	273.0	0
76	47	47.8	1.7	47.2	0.4

#### 4. POROSITY DETERMINATION

Porosity values were determined using a helium pycnometer (Micromeritics Accupyc 1330). The measuring method is based on the exact determination of the amount of Helium gas displaced by a samples solid phase volume. Prior to and after each experiment, a weighed sample was placed in a test cell with known volume. The gas pressures observed upon filling the measuring chamber and then discharging it into a second empty chamber allow the determination of volume displaced ( $V_{pyc}$ ). Since the geometrical volume ( $V_g$ ) of the cylindrical sample is known, the volumetric fraction of the rock's connected porosity ( $\Phi$ ) can be estimated using

$$\Phi = (V_g - V_{pyc})/V_g \quad (3).$$

In our experiments we observe that, in contrast to deformation in the purely viscous and/or plastic regime at low applied stress (Lavallée et al., 2007), the failure of magma is accompanied by an increase in porosity, although no systematic increase is noted with applied stress (Table DR2). We surmise that such a lack of correlation between the applied stress and the changes in the porous network may reflect the difficulty in arresting the deformation at a comparable total strain prior to failure for each experimental condition.

**Table DR2.** Physical property changes induced by magma deformation. Porosity ( $\Phi$ ) measurements were done at room temperature, using a helium pycnometer (Micromeritics Accupyc 1330). \*The porosity of the sample deformed at an applied stress of 76 MPa was exceptionally measured via the Archimedean method as the deformed sample would not fit in the pycnometer. P- and S-wave ultrasonic velocities were measured using a pulsing signal at 50 dB, monitored across the sample by an oscilloscope. The post-experiments values are compared to the average velocities of  $3.13 \pm 0.03$  km/s obtained for the P-waves and  $1.55 \pm 0.09$  km/s obtained for the S-wave of the original rock sample.

Applied stress (MPa)	Strain (%)	$\Phi_{\text{before}}$ (%)	$\Phi_{\text{after}}$ (%)	$\Delta\Phi$ (%)	$V_{p\text{after}}$ (Km/s)	$V_{s\text{after}}$ (km/s)	$\Delta P$ - (%)	$\Delta S$ - (%)
8	35	6.7	5.7	-1.0	3.03	1.54	-3.2	-0.6
28.5	18	6.9	21.0	+14.1	2.00	1.22	-36.1	-21.3
46	12	7.3	18.2	+10.9	1.87	1.06	-40.3	-31.6
76	5.5	7.1	28.0*	+20.9	1.92	1.01	-38.7	-34.8

## 5. ULTRASONIC TESTING

Pre- and post-experiment ultrasonic wave velocities were measured via PZT piezoelectric P- and S-wave transducer crystals positioned at each end of the sample, using a Agilent Technologies 1.5GHz 'Infiniium' digital storage oscilloscope and a JSR DPR300 35MHz ultrasonic pulser/receiver. The cylindrical sample was positioned lengthwise between a set of transducers (P or S) and a 900V pulse was discharge from a pulsing transducer across the sample and simultaneously to the oscilloscope. Time of arrivals of P- (or S-) wave to the receiving transducer as well as the length of the sample was used to calculate each ultrasonic velocity.

Deformation in the ductile-brittle transition is accompanied by a decrease in P- and S-wave velocities (Table DR2), which may be associated with the creation of damage through fracturing of the samples. In contrast, deformation in the purely viscous and/or plastic regime at low applied stress (Lavallée et al., 2007), results in nearly no changes in ultrasonic velocities.

## 6. NEUTRON COMPUTED TOMOGRAPHY

The internal structure of the samples was analysed prior to deformation and following failure using a novel neutron computed tomography (NCT) method. This method is identical – in principle – to X-ray computed tomography, which is widely used in medical science, and becoming more popular in the geosciences due to the 3-D, but non-destructive nature of the resulting analysis (Ketcham and Carlson, 2001). One of the advantages of the neutron over X-ray is that it enables the imaging of

large samples up to 36 cm. Imaging was carried out using the ANTARES detector and FRM II cold neutron beam facility installed at Garching, Germany (Hess et al., 2011). Reconstructed images from the NCT have a voxel size of approximately 20  $\mu\text{m}$ , easily permitting a 3-D reconstruction of the internal structure of the samples and the extensive fracture patterns produced by the deformation (Hess et al., 2011; King et al., 2008).

### 7. 3-D RECONSTRUCTION OF THE FRACTURING ARCHITECTURE

Reconstruction videos of the internal fracture networks were produced for samples deformed at 28.5 and 76 MPa (Video DR1). The videos show the cross sectional structures, traveling downward through the samples.

**Movie DR1.** Videos of the internal, permeable, fracture network structure of experimentally deformed samples from top to bottom. The crystals and glass show in a grey scale and the fractures show in black. (A) Under 28.5 MPa, radial, extensional cracks dominate the brittle response of the sample. (B) Under 76 MPa, deformation is mainly brittle and primarily forced the propagation of major shear cracks.

### 8. FRACTURE NETWORK DISTRIBUTION

The distribution of fractures was quantified by assessing their geometries and positions. The volume of crack space was delimited by thresholding the greyscale tomography data for the air and simply summing up the voxels together. After identification, the widths of cracks were determined using an n-space Euclidean distance algorithm combined to a topological skeletonisation to find the centre of the crack (e.g., Ma and Sonka, 1996). The distribution of cracks was quantified with respect to their radial orientation – a practice, equivalent to a 2D anisotropy, possible due to the general cylindrical symmetry of cracks produced in a cylindrical sample deformed uniaxially. For each skeleton line in a 2D cylindrical cross section (Fig. S7), the radial extent  $r$  and length  $l$  are measured and the ratio provides the radial orientation  $\nu$ .

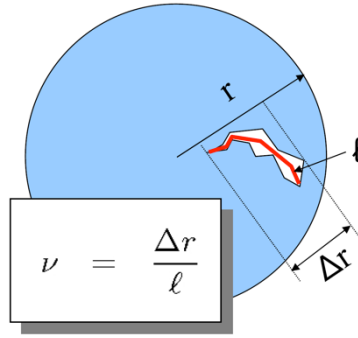


Figure DR7. Schematics of fracture dimension quantification.  $\Delta r$ : radial extent,  $l$ : length, and  $\nu$ : the ratio provides the radial orientation.

In a second step, the area of each fracture was estimated using the amount of black voxels covered. Finally the density of fractures for a given location into a sample's half space was computed, which provided us with the illustrations in Figure 1 of the main text.

## 9. PERMEABILITY ANALYSIS

The permeability ( $\kappa$ ) of lava dome rocks can be approximated through their porosity ( $\phi$ ) as they yield the following (Mueller et al., 2005):

$$\kappa = 10^{-17} \phi^{3.4} \quad (4).$$

This relationship combined with the crack densities imaged by NCT (Bai et al., 2011; Hess et al., 2011; e.g., Pan et al., 2010) can thus provide a first order map of the permeability development during magma failure. Although the total porosity increases by cracking were comparable and led to similar bulk permeability increase (Table DR2), analysis of the directional crack density from the NCT results highlighted contrasting anisotropy of the fracture networks in the different experiments. Flow in an anisotropic medium is very sensitive to fracture intensity ( $P$ ) that defines the number of fractures expressed as

$$P = A_F/V \quad (5)$$

where  $A_F$  is the total area of the fracture contained in a volume ( $V$ ) (Pan et al., 2010). The parameter  $P$  defines the number of fracture per unit length and is scale invariant (Ortega et al., 2006). When considering the anisotropy of a fracture network with a known volume, such as in our experimental samples, the fracture intensities in the axial ( $a$ ) and lateral ( $l$ ) directions respectively scales with the surface area of cracks in each direction. Assuming that the surface area of fracture in a direction is a proxy for the permeable porosity in this direction – thus approximated by the ratio of area of fracture to considered surface area ( $A_T$ ) – equation 4 can be reformulated to estimate the permeability along the axis of the samples ( $\kappa_a$ ) and laterally across the sample ( $\kappa_l$ ):

$$\kappa_a = 10^{-17} \left( \frac{A_{Fa}}{A_{Ta}} \right)^{3.4} \quad (6)$$

and



$$\kappa_l = 10^{-17} \left( \frac{A_{Fl}}{A_{Tl}} \right)^{3.4} \quad (7),$$

where  $A_{Fa}/A_{Ta}$  and  $A_{Fl}/A_{Tl}$  are estimated from tomography transects orthogonal to the axial and a radial direction, respectively (Fig. DR8).

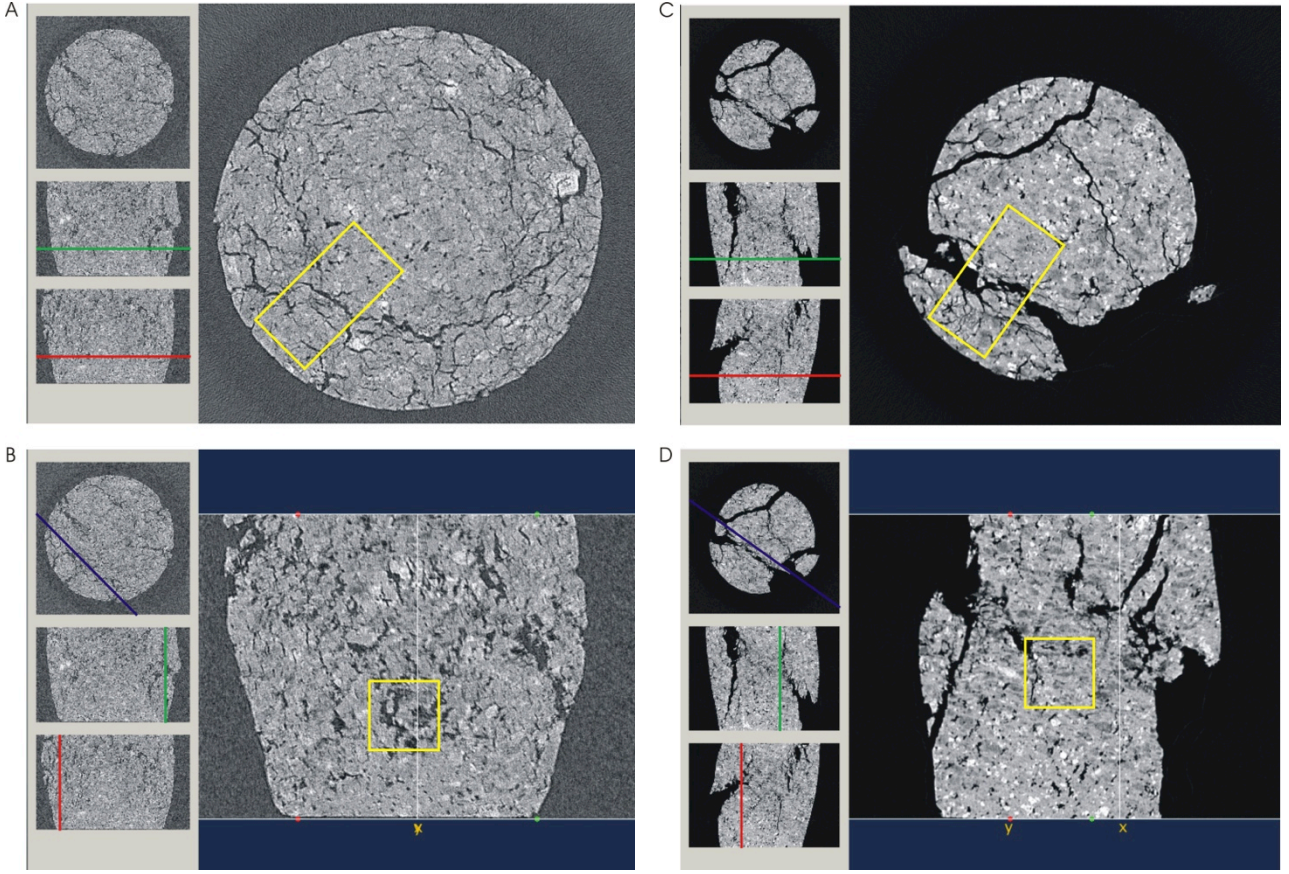


**Figure DR8. Reconstruction of the permeable fracture network.** Regions from which the permeability was estimated across a segment of shear zone. The blue, green and red lines indicate the position of the sections of images displayed. A-B) The porosity of sample deformed at 28.5 MPa was estimated in a volume of 250 mm<sup>3</sup> (Yellow boxes). The analysis was performed in A) the axial direction of the sample, perpendicular to the applied stress, and in B) the radial direction, orthogonal to the applied stress. C-D) The porosity of sample deformed at 76 MPa was estimated in a volume of 250 mm<sup>3</sup> (Yellow boxes). The analysis was performed in C) the axial direction of the sample, perpendicular to the applied stress, and in D) the radial direction, orthogonal to the applied stress.

Tomographic sections were converted to binary images (pores and cracks were converted to black and the rock was converted to white) and the images were analysed with the JMicroVision toolbox (Roduit, 2006). The analysed porosities were then converted to permeabilities using equations 6 and 7 (Table DR3).

Table DR3. Permeability estimated on the basis of the porosity analysis. The data are plotted on Figure 2 in the main text.

Sample	Spatial analysis	Porosity	Permeability
<b>28.5 MPa</b>	<i>Bulk rock</i>	21 %	$3.1 \times 10^{-13}$
	<i>Axial</i>	19.1%	$2.3 \times 10^{-13}$
	<i>Lateral</i>	33.2	$1.5 \times 10^{-12}$
<b>76 MPa</b>	<i>Bulk rock</i>	28 %	$1.3 \times 10^{-12}$
	<i>Axial</i>	32.4 %	$3.4 \times 10^{-12}$
	<i>Lateral</i>	16.0 %	$1.2 \times 10^{-13}$

## 10. POST-EXPERIMENT MICROSTRUCTURAL ANALYSIS

The damage induced in the magma was further imaged using the traditional method of microscopic analysis. During thin section preparation, the rock samples were impregnated with epoxy doctored by the presence of a fluorescent dye in order to highlight the permeable, porous network (Fig. S9). Mosaics of microphotographs ( $n > 150$ ) of the thin sections taken under reflected ultraviolet light illustrate at a high resolution the localisation of fractures during deformation at high applied stress (Fig DR9 above). Moreover, the mosaics of the microphotographs taken under combined, reflected ultraviolet light and transmitted normal light display the relationship harboured between the propagation of fractures and the presence of phenocrysts (Fig DR9 middle). We note that phenocrysts are especially fractured in the material that has undergone a more significant amount of strain before ensuing to failure (i.e., at lower applied stress) (Fig DR9 below). This observation further leads us to suggest that during relatively “slow” failure (e.g., at an applied stress of 28.5 MPa) strain dissipate and is accommodated brittly by phenocrysts, which crack and enhance the contribution to the permeable porous network, whereas during relatively “fast” failure (e.g., at an applied stress of 76 MPa), the development of cracks occurs (nearly) irrespective of the phenocrysts. From these observation, we conclude that the path dependence of failure (i.e., the total strain to failure) is material is strongly influenced by the presence of phenocrysts.



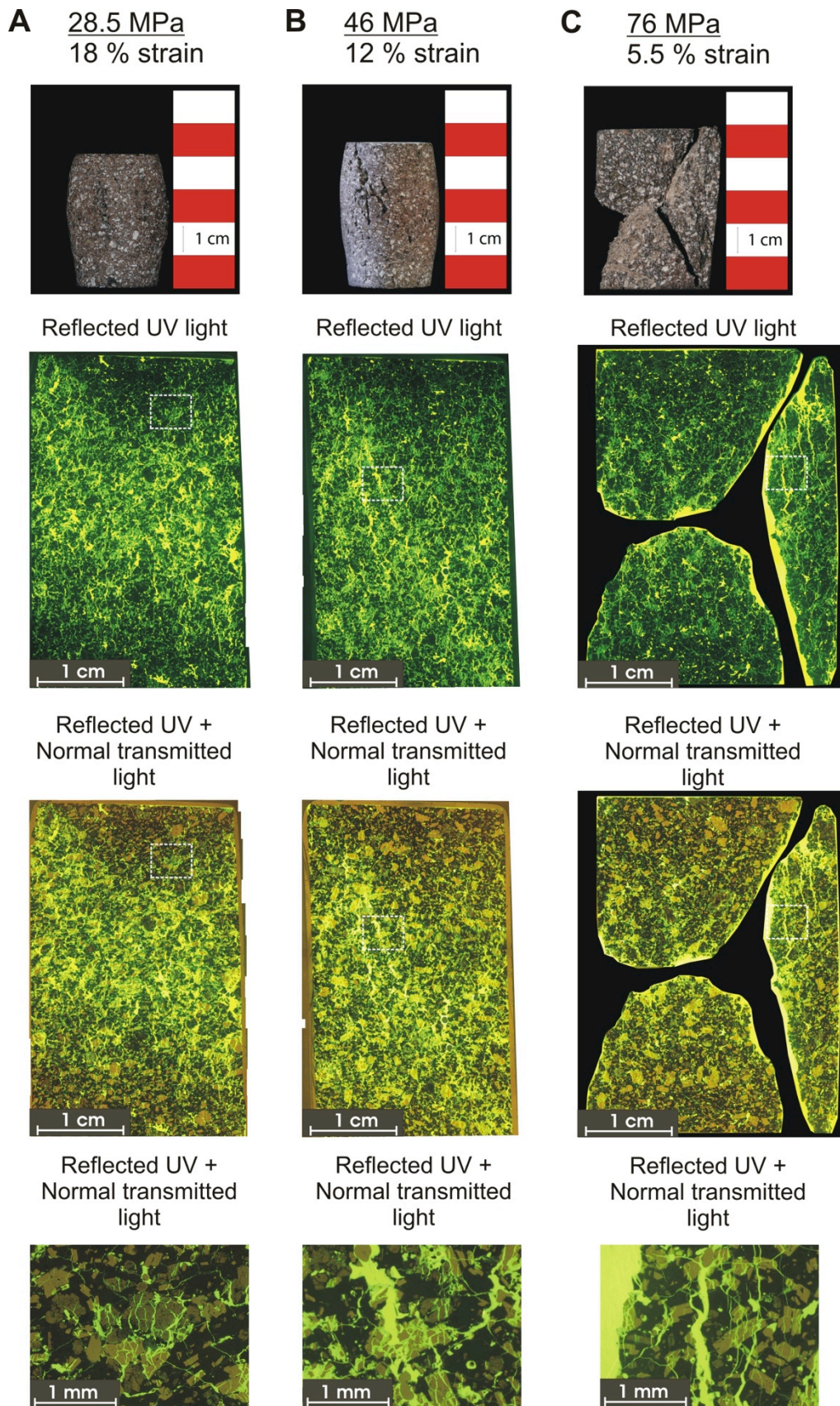


**Figure DR9. Microstructures produced during magma failure at A) 28.5 MPa, B) 46 MPa, and C) 76 MPa.** The photograph of each sample is accompanied by a set mosaics of microphotographs taken under reflected UV light (above) and combined, reflected UV light and normal transmitted light (middle). These mosaics highlight the increase localisation of cracks with applied stress. Each mosaic further contains an inset box in which a high-resolution microphotographs display the relationship between cracking and the phenocrysts. [Note: for the sample deformed at 76 MPa, the localised macroscopic cracks prevented us from making one thin section for the rock, as the sample was very fragile. We thus prepared three different thin sections and reconstructed the sample geometry.]

## SUPPLEMENTARY INFORMATION REFERENCES

- Aki, K., 1965, Maximum likelihood estimate of  $b$  in the formula  $\log N = a - bm$  and its confidence limits: Bulletin of the earthquake research institute, Tokyo University, v. 43, p. 237-239.
- , 1967, Scaling law of seismic spectrum: Journal of Geophysical Research, v. 72, no. 4, p. 1217-&.
- Bai, L. P., Baker, D. R., and Hill, R. J., 2011, Permeability of vesicular Stromboli basaltic glass: Lattice Boltzmann simulations and laboratory measurements: Journal of Geophysical Research-Solid Earth, v. 115.
- Cornelius, R. R., and Voight, B., 1995, Graphical and Pc-Software Analysis of Volcano Eruption Precursors According to the Materials Failure Forecast Method (FFM): Journal of Volcanology and Geothermal Research, v. 64, no. 3-4, p. 295-320.
- Gerik, A., and Kruhl, J. H., 2008, Towards automated pattern quantification: time-efficient assessment of anisotropy of 2D patterns with AMOCADO: Computers and Geosciences.
- Hess, K. U., Cordonnier, B., Lavallée, Y., and Dingwell, D. B., 2007, High-load, high-temperature deformation apparatus for synthetic and natural silicate melts: Review of Scientific Instruments, v. 78.
- Hess, K. U., Flaws, A., Schillinger, B., Mühlbauer, M., Schulz, M., Calzada, E., and Dingwell, D. B., 2011, Applications of a high to ultra-high resolution neutron computed tomography system for the geosciences: Geological Society of America Bulletin, v. Advances in 3-D imaging and analysis of geomaterials, no. Geosphere Themed Issue.
- Ketcham, R. A., and Carlson, W. D., 2001, Acquisition, optimization and interpretation of X-ray computed tomographic imagery: applications to the geosciences: Computers & Geosciences, v. 27, no. 4, p. 381-400.
- Kilburn, C. R. J., 2003, Multiscale fracturing as a key to forecasting volcanic eruptions: Journal of Volcanology and Geothermal Research, v. 125, no. 3-4, p. 271-289.
- King, A., Johnson, G., Engelberg, D., Ludwig, W., and Marrow, J., 2008, Observations of intergranular stress corrosion cracking in a grain-mapped polycrystal: Science, v. 321, no. 5887, p. 382-385.
- Lavallée, Y., Benson, P. M., Heap, M. J., Flaws, A., Hess, K. U., and Dingwell, D. B., 2012a, Volcanic conduit failure as a trigger to magma fragmentation: Bulletin of Volcanology, v. 74, no. 1, p. 11-13.
- Lavallée, Y., Hess, K. U., Cordonnier, B., and Dingwell, D. B., 2007, A non-Newtonian rheological law for highly-crystalline dome lavas: Geology, v. 35, p. 843-846.
- Lavallée, Y., Meredith, P., Dingwell, D. B., Hess, K. U., Wassermann, J., Cordonnier, B., Gerik, A., and Kruhl, J. H., 2008, Seismogenic lavas and explosive eruption forecasting: Nature, v. 453, no. 22 May, p. 507-510.
- Lavallée, Y., Varley, N., Alatorre-Ibargüengoitia, M. A., Hess, K.-U., Kueppers, U., Mueller, S., Richard, D., Scheu, B., Spieler, O., and Dingwell, D. B., 2012b, Magmatic Architecture of Dome-Building Eruptions at Volcán de Colima, Mexico: Bulletin of Volcanology, v. 74, no. 1, p. 249-260.
- Ma, C. M., and Sonka, M., 1996, A fully parallel 3D thinning algorithm and its applications: Computer Vision and Image Understanding, v. 64, no. 3, p. 420-433.
- McNutt, S. R., 2005, Volcanic seismology: Annual Review of Earth and Planetary Sciences, v. 33, p. 461-491.
- Mueller, S., Melnik, O., Spieler, O., Scheu, B., and Dingwell, D. B., 2005, Permeability and degassing of dome lavas undergoing rapid decompression: An experimental determination: Bulletin of Volcanology, v. 67, no. 6, p. 526-538.
- Ortega, O. J., Marrett, R. A., and Laubach, S. E., 2006, A scale-independent approach to fracture intensity and average spacing measurement: Aapg Bulletin, v. 90, no. 2, p. 193-208.
- Pan, J.-B., Lee, C.-C., Lee, C.-H., Yeh, H.-F., and Lin, H.-I., 2010, Application of fracture network model with crack permeability tensor on flow and transport in fractured rock: Engineering Geology, v. 116, no. 1-2, p. 166-177.
- Reubi, O., and Blundy, J., 2008, Assimilation of Plutonic Roots, Formation of High-K Exotic Melt Inclusions and Genesis of Andesitic Magmas at Volcán De Colima, Mexico: Journal of Petrology, v. 49, no. 12, p. 2221-2243.
- Roduit, N., 2006, JMicroVision: Image analysis toolbox for measuring and quantifying components of high-definition images.
- Savov, I. P., Luhr, J. F., and Navarro-Ochoa, C., 2008, Petrology and geochemistry of lava and ash erupted from Volcan Colima, Mexico, during 1998-2005: Journal of Volcanology and Geothermal Research, v. 174, no. 4, p. 241-256.
- Smith, R., and Kilburn, C. R. J., 2010, Forecasting eruptions after long repose intervals from accelerating rates of rock fracture: The June 1991 eruption of Mount Pinatubo, Philippines: Journal of Volcanology and Geothermal Research, v. 191, p. 129-136.
- Voight, B., 1988, A Method for Prediction of Volcanic-Eruptions: Nature, v. 332, no. 6160, p. 125-130.